

Optimization of quantitative susceptibility mapping for regional estimation of oxygen extraction fraction in the brain

John J. McFadden¹  | Julian C. Matthews¹ | Lauren A. Scott¹  |
Geoff J. M. Parker^{2,3}  | Maélène Lohéziec⁴ | Laura M. Parkes^{1,5} 

¹Division of Neuroscience and Experimental Psychology, School of Biological Sciences, Faculty of Biology, Medicine, and Health, University of Manchester, Manchester Academic Health Science Centre, Manchester, United Kingdom

²Bioxydyn Limited, Manchester, United Kingdom

³Centre for Medical Image Computing, Department of Computer Science and Department of Neuroinflammation, University College London, London, United Kingdom

⁴Applications & Workflow, GE Healthcare, Manchester, United Kingdom

⁵Geoffrey Jefferson Brain Research Centre, Manchester Academic Health Science Centre, Manchester, United Kingdom

Correspondence

John J. McFadden, Division of Neuroscience and Experimental Psychology, School of Biological Sciences, Faculty of Biology, Medicine, and Health, University of Manchester, Manchester Academic Health Science Centre, R124e, Zochonis Building, Oxford Road, Manchester, M13 9GB, UK.
Email: john.mcfadden@postgrad.manchester.ac.uk

Funding information

GE Healthcare; Engineering and Physical Sciences Research Council, Grant/Award Number: EP/M005909/1

Purpose: We sought to determine the degree to which oxygen extraction fraction (OEF) estimated using quantitative susceptibility mapping (QSM) depends on two critical acquisition parameters that have a significant impact on acquisition time: voxel size and final echo time.

Methods: Four healthy volunteers were imaged using a range of isotropic voxel sizes and final echo times. The 0.7 mm data were downsampled at different stages of QSM processing by a factor of 2 (to 1.4 mm), 3 (2.1 mm), or 4 (2.8 mm) to determine the impact of voxel size on each analysis step. OEF was estimated from 11 veins of varying diameter. Inter- and intra-session repeatability were estimated for the optimal protocol by repeat scanning in 10 participants.

Results: Final echo time was found to have no significant effect on OEF. The effect of voxel size was significant, with larger voxel sizes underestimating OEF, depending on the proximity of the vein to the superficial surface of the brain and on vein diameter. The last analysis step of estimating vein OEF values from susceptibility images had the largest dependency on voxel size. Inter-session coefficients of variation on OEF estimates of between 5.2% and 8.7% are reported, depending on the vein.

Conclusion: QSM acquisition times can be minimized by reducing the final echo time but an isotropic voxel size no larger than 1 mm is needed to accurately estimate OEF in most medium/large veins in the brain. Such acquisitions can be achieved in under 4 min.

KEYWORDS

oxygen extraction fraction, quantitative susceptibility mapping, susceptibility weighted imaging, venous saturation

This is an open access article under the terms of the Creative Commons Attribution License, which permits use, distribution and reproduction in any medium, provided the original work is properly cited.

© 2021 The Authors. *Magnetic Resonance in Medicine* published by Wiley Periodicals LLC on behalf of International Society for Magnetic Resonance in Medicine

1 | INTRODUCTION

Non-invasive imaging measurements of brain oxygenation have wide potential scientific and clinical utility, for example in Alzheimer disease, stroke, and Parkinson disease.¹⁻³ Quantitative susceptibility mapping (QSM) is a promising approach to estimate oxygen extraction fraction (OEF) but cross-comparisons of studies are undermined by the absence of a set of standard, optimized acquisition parameters and recommended analysis methods. Establishment of a consistent protocol is also critical for multi-center research studies. The development of a set of recommendations is likely to be a prerequisite to the adoption of these techniques to common clinical use. While the endpoint of this process will require a consensus opinion as has been achieved for the use of arterial spin labeling for the estimation of cerebral blood flow (CBF),⁴ to get to this point the effects of acquisition parameters on the accuracy of the OEF estimation needs to be determined.

If it is assumed that magnetic susceptibility within veins is predominately from deoxygenated hemoglobin, QSM can provide an estimate of venous oxygen saturation (SvO₂). OEF can then be estimated according to⁵:

$$OEF = \frac{SaO_2 - SvO_2}{SaO_2} \quad (1)$$

where SaO₂ is oxygen saturation within arterial blood, typically measured using pulse oximetry or assumed to have a value of 100%. If CBF (mL blood/min/100 g) to the region is also known then the cerebral metabolic rate of oxygen consumption (CMRO₂ in mmol O₂/min/100 g) can be estimated:

$$CMRO_2 = CBF \cdot [O_2]_a \cdot OEF \quad (2)$$

where [O₂]_a is the concentration of oxygen within arterial blood (in mmol O₂/mL blood).

Regional OEF measured along with CBF and CMRO₂ using oxygen-15 positron emission tomography (PET) have shown some disease processes are likely to impact oxygen extraction on a regional basis.^{1,3,6-8} This technique is not translatable to wide clinical use due to its high cost and the challenging methodology of administering radioactivity with a half-life of 2 min. Alternative approaches have been developed using MRI such as dual-calibrated fMRI⁹⁻¹¹ and quantitative BOLD¹² but these in general entail long acquisition times and/or gas challenge and use of physiological assumptions in the modelling that may not hold in disease. T₂-relaxation-under-spin-tagging (TRUST) is the most widely used technique which relates the T₂ of blood to oxygen saturation,¹³⁻¹⁵ with a growing literature investigating its sensitivity to disease-related changes.^{16,17} TRUST requires spin labelling of venous blood, generally limited to global

measurements taken from the superior sagittal sinus (SSS) to achieve sufficient signal-to-noise ratio (SNR). A recent attempt to provide regional information applied selective localisation of the T₂ encoding prior to spin labeling, successfully demonstrating hemispherical specificity.¹⁸ This would have utility for conditions such as stroke but may not be able to resolve smaller regions of interest in neurodegenerative disease. High resolution QSM may provide a better approach to estimate regional OEF from SvO₂ estimation inside smaller veins. OEF can also be estimated using susceptibility-based oximetry (SBO)¹⁹ but this approach is restricted to straight vessels and is sensitive to the angle of the vessel to the external field, with measurements, therefore, generally restricted to the SSS. QSM is essentially an extension of SBO, allowing quantification of OEF for veins of arbitrary geometry and orientation, making it more suitable for regional OEF estimation.

QSM reconstructs a voxel-wise map of susceptibility from the phase information. Susceptibilities of venous blood-only voxels can be used to calculate vessel-specific SvO₂ from:

$$\Delta\chi_{vein-CSF} = (1 - SvO_2) \cdot \Delta\chi_0 \cdot Hct + (\Delta\chi_{Hb-H_2O} \cdot Hct) \quad (3)$$

where $\Delta\chi_{vein-CSF}$ is the susceptibility difference between the vein and cerebrospinal fluid (CSF) in ppm, $\Delta\chi_{Hb-H_2O}$ is the susceptibility difference between fully oxygenated red blood cells and water (-0.03 parts per million (ppm) in cgs [centimeter/gram/second] units),²⁰ *Hct* is the hematocrit, and $\Delta\chi_0$ is the susceptibility difference per unit hematocrit between fully oxygenated and fully deoxygenated red blood cells (0.27 ppm in cgs units).²¹ The first term on the right hand side of Equation (3) expresses the susceptibility contribution due to the relative proportion of deoxygenated to oxygenated red blood cells, and the second term a smaller contribution due to the susceptibility difference between oxygenated red blood cells and water.

QSM-derived OEF estimates have been compared to those from PET in arterial stenosis²² and show expected sensitivity to caffeine, hyperoxia, hypercapnia, and acetazolamide.²³⁻²⁶ However, the long acquisition times used for high resolution regional OEF²⁷ and a lack of consensus on optimal scanning parameters hinder translation of QSM to clinical practice and undermine comparisons between studies.

Here, we investigate the impact on OEF estimates of minimizing acquisition times by increasing voxel size and reducing the longest or final echo time in a range of vein sizes and locations. The increase in acquisition time with voxel size follows an inverse power relationship (10 min for 0.7 mm isotropic voxel size compared with approximately 4 min for a 1 mm voxel size), and a linear relationship with final echo time (approximately 4 min for 12 ms and 7 min for 32 ms when using 1 mm voxels).

Larger voxel sizes could impact OEF accuracy in a number of ways including: (1) the degree of discretization of the

phase image and the consequential reduction in phase contrast, due to the enhanced voxel sensitivity function mixing effect²⁸; (2) the degree of discretization of the phase image and the impact this has on global processing steps including background field estimation, phase unwrapping, and dipole inversion; (3) the greater SNR of the phase images; (4) increase in size of the point spread function; (5) worse Gibbs ringing; and (6) the greater partial volume of tissue and vein within the voxel. We simulated the effects of acquiring at different size matrices by performing spatial downsampling on the highest resolution data at different stages of processing and compared the resultant OEF estimates to determine the relative impact of voxel size at each processing step, and whether the impact is different for deep and superficial veins. This will only simulate a subset of the potential impacts above associated with acquiring at different voxel sizes (namely (1) to (3) and (6)) but comparison of OEF estimation between simulated and acquired data will determine the relative importance of the other factors.

QSM fits the phase against the echo time on a voxelwise basis, enabling the total field to be estimated. The quality of the fit can be expected to improve with (1) a larger number and (2) a wider range of TEs and so both these factors will likely have an impact on both the accuracy and precision of the OEF estimate. The OEF-dependent signal within veins will decrease relatively quickly with increasing echo time and so a shorter final echo time may be sufficient compared to what is optimal for tissue susceptibility estimation where T_2^* is longer. Extending the final echo time beyond a certain limit may be detrimental if there is no signal left and the data are simply adding noise. However additional echoes up to this final echo time can only be beneficial, as they will clearly add more signal than noise, and with a multi-echo sequence these are essentially obtained “for free.” Hence, we decided

to study the impact of final echo time only and maximise the number of echoes up to this point as would always be beneficial in practice.

For our optimized acquisition protocol, we collected test re-test data from 10 people in order to determine the inter-session repeatability of the OEF estimates in a range of vein sizes and locations. Intra-session repeatability was assessed in a single participant by seven repeat scans in a single session.

2 | METHODS

2.1 | Data acquisition

The University of Manchester research ethics committee approved this study and written informed consent was obtained from all participants.

Whole brain images were collected in four healthy volunteers (age range 23-25, two males) using a sagittal 3D multi-echo gradient echo sequence at 3T (Signa PET/MR, GE Healthcare, Waukesha, WI) and a 32-channel head coil (Nova Medical, Wilmington, MA), with common parameters of: field of view (FOV) = 20.8 cm × 20.8 cm × 15.6 cm; bandwidth (BW) = ±62.5 kHz; flip angle = 15°; ASSET factor = 2 (phase encoding only), with phase encoding in the anterior-posterior direction and a bipolar echo collection scheme. Bipolar flow compensation gradients are included before each echo in the slice encoding direction to null the first order gradient moment. In addition, flow compensation is achieved in the frequency encoding direction through application of a moment nulling gradient before the first echo. A Hanning filter was applied but half-Fourier/partial k-space was not. The isotropic voxel dimensions used to investigate the influence of voxel size are listed in Table 1 alongside

TABLE 1 Imaging parameters and acquisition times used to investigate the effects of voxel size and final echo time

Voxel size (mm)	#Slices	Matrix size	#TEs	First TE (ms)	Final TE (ms)	ΔTE (ms)	TR (ms)	Acquisition time (m:s)
0.7	222	298 × 298	6	3.9	17.2	2.7	25.8	10:07
1	156	208 × 208	8	3.0	16.5	2.0	22.7	04:19
1.5	104	138 × 138	10	2.2	14.5	1.4	19.3	01:40
1.8	86	116 × 116	12	2.0	15.1	1.2	18.9	01:10
2	78	104 × 104	12	1.9	13.9	1.1	17.7	00:54
2.5	62	84 × 84	14	1.7	13.8	0.9	17.3	00:34
3	52	70 × 70	16	1.5	13.9	0.8	17.0	00:25
1	156	208 × 208	6	3.0	12.6	1.9	18.9	03:34
1	156	208 × 208	10	3.0	20.3	1.9	26.4	05:01
1	156	208 × 208	12	3.0	24.2	1.9	30.3	05:44
1	156	208 × 208	14	3.0	28.0	1.9	34.1	06:27
1	156	208 × 208	16	3.0	31.9	1.9	37.9	07:10

Abbreviation: TE, echo time; TR, repetition time.

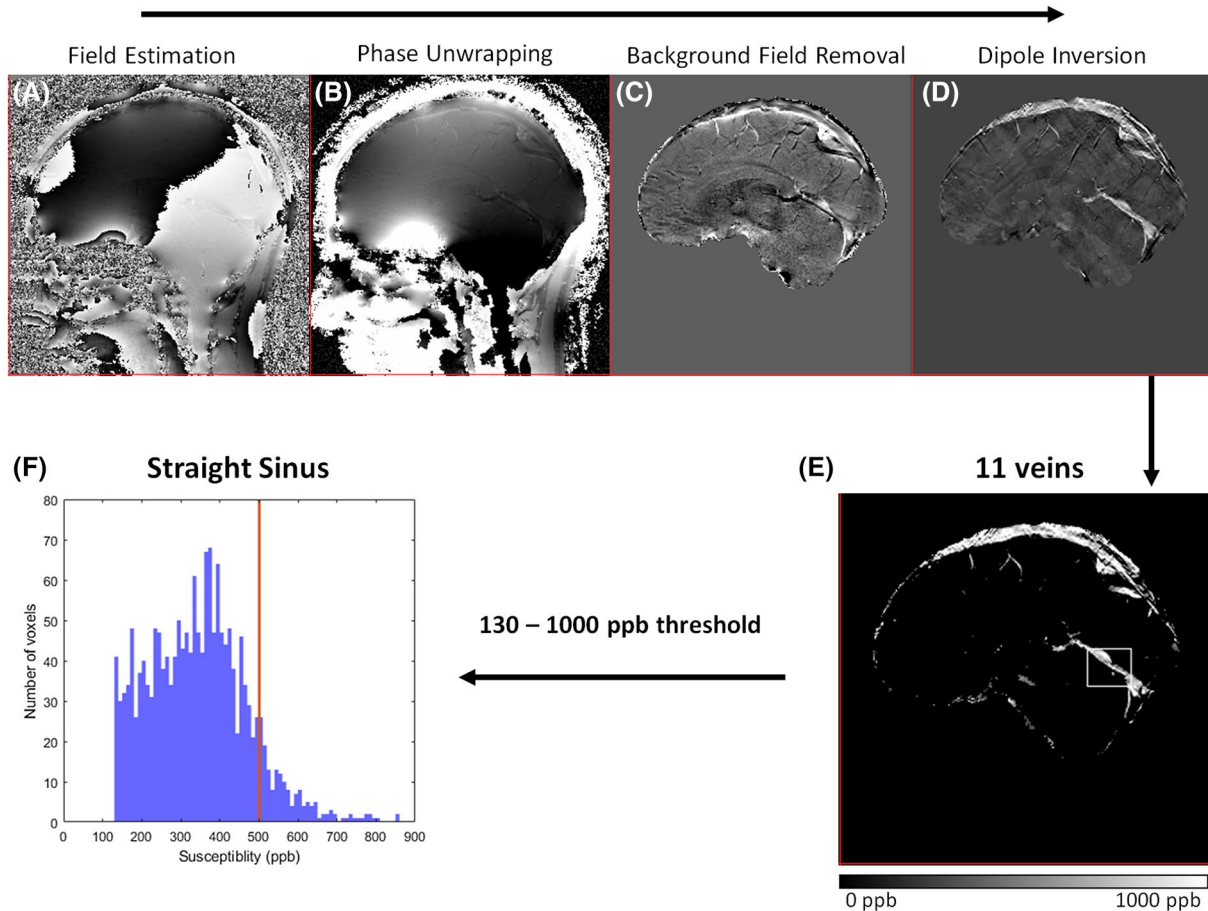


FIGURE 1 Flowchart describing implementation of QSM venography. Susceptibility maps were calculated using the processing steps of field estimation (A), phase unwrapping (B), background field removal (C), and dipole inversion (D). E, The resultant susceptibility map was thresholded to between 130 and 1000 ppb and a non-oblique cuboid (of variable size depending on the vein anatomy and surroundings) was placed on each of 11 major veins, example of SS shown here. F, The histogram of the susceptibility values from voxels inside the cuboid and threshold limits was analyzed and the 90th percentile, represented by the red line, was used to estimate the susceptibility of the corresponding vein

their associated echo time parameters and acquisition times. As the minimum echo spacing reduces with increasing voxel size, the number of echoes was set so that the final echo times of each protocol were as similar as possible. This, therefore, captures the true gain (in terms of additional echoes) that would be made in practice by increasing the voxel size while maintaining the final echo time. The 1 mm voxel size acquisition was repeated on each person while varying the number of echoes and, therefore, final echo time from 6 to 16 echoes in steps of two, as outlined in the bottom half of Table 1. All four people were scanned with this complete protocol with the individual sequence parameters as shown in the rows in Table 1 applied in a randomized order. Intra-session precision was also estimated in one of the subjects by repeating the 1-mm six-echo protocol (Table 1, eighth row) seven times in a separate session.

Inter-session repeatability was estimated by repeat scanning of 10 people with mild cognitive impairment (MCI) (age range 60–80 y, 5 male) with an interval of 12 ± 12 days apart using the 1-mm six-echo protocol (Table 1 eighth row).

Caffeine intake was controlled by instructing people not to consume any caffeinated drinks on the day of the scan. A venous blood sample was taken approximately 30 min prior to the scan from which *Hct* was measured. SaO_2 was measured using a pulse oximeter placed on the index finger and values were recorded every minute during the QSM scan.

Scanner-reconstructed, post-coil combination magnitude, real, and imaginary images were collected in all cases. Images were not spatially interpolated during the reconstruction process.

2.2 | Quantitative susceptibility mapping data analysis

All image manipulations were performed in Matlab (v2017a, The MathWorks, Inc., Natick, MA). Prior to any image processing, each acquired dataset was partitioned by echo polarity with odd or even echo datasets analysed separately. Susceptibility maps from the collected data were calculated

from the real and imaginary data as shown in Figure 1 using the following QSM pipeline in MEDI+0^{29,33} (Cornell MRI Research Lab) and FSL³⁴ with default parameters unless otherwise stated using the following processing steps:

Step 1: Total field estimation from voxel-wise quadratic fitting of signal evolution against TE^{29,35,36} (Figure 1A) and phase unwrapping using region growing³⁷ (Figure 1B) producing a total field map.

Step 2: Background field removal using projection-onto-dipole-fields^{30,38} (Figure 1C) after brain masking using the brain extraction tool in FSL,³⁹ producing a local field map.

Step 3: Dipole inversion using Morphology-Enabled-Dipole-Inversion (MEDI) (Figure 1D) incorporating the local field map and magnitude image to produce a quantitative susceptibility map. Dipole inversion made use of the ventricles as a reference region, delineated automatically using a thresholded R_2^* map.³¹ The final susceptibility maps from the odd and even echoes were then averaged.

Step 4: A semi-automated method was developed to extract venous voxels that are predominately blood from which OEF values for these vessels were estimated, which is detailed in the next section.

2.3 | Semi-automated vein selection

For all calculated maps, a 3D single iteration erosion algorithm developed in-house removed the outermost voxels at the edge of the brain to minimize tissue-air boundary errors resulting from imperfect background field removal. Venous regions of interest (ROIs) were then isolated using a lower boundary of 130 ppb (parts per billion) and an upper boundary of 1000 ppb to mask the image,²⁷ (Figure 1E). For the optimization study, 11 veins of varying geometries, locations, and orientations were selected from an anatomical textbook⁴⁰ on the basis of their large size and prominence, and are summarized in Table 2. They were manually located on the 0.7 mm thresholded map by placing a non-oblique cuboid ROI across multiple slices, taking all thresholded voxels within the ROI as belonging to the vein following visual inspection. Figure 1E shows the ROI corresponding to the straight sinus (SS). The vein ROIs determined on the 0.7 mm map were then resized and applied to the thresholded lower resolution maps, rounding the cuboid dimensions to the nearest whole number.

2.4 | Vein OEF estimation

The 90th percentile of non-zero voxels within each vein ROI was used to estimate the susceptibility in the corresponding

TABLE 2 Veins included in the analysis

Vein location category	Abbreviation	Vein
Deep	SS	Straight Sinus
	VoG	Vein of Galen
	ICVs	Internal Cerebral Veins
	ISS	Inferior Sagittal Sinus
	SCV	Small Cerebral Vein
Superficial	SSS \parallel	Superior Sagittal Sinus (approximately parallel to B_0)
	SSS \perp	Superior Sagittal Sinus (approximately perpendicular to B_0)
	SAV	Superior Anastomatic Vein
	LTS	Left Transverse Sinus
	RTS	Right Transverse Sinus
	IAVL	Inferior Anastomatic Vein of Labbé

SCV is a perpendicular tributary of the SSS located anterior to the precentral gyrus with a similar diameter and orientation across all subjects.

vein (Figure 1F), a process which was done independently for each resolution. If there were fewer than 10 non-zero voxels in the ROI, the result was discarded. A subset of six veins that could be reliably identified on the 1 mm voxel size image was used for the intra- and inter-session repeatability studies: SS, vein of Galen (VoG), SSS \parallel , SSS \perp , internal cerebral vein (ICV), and the largest transverse sinus.

The susceptibility values were then converted to an estimate of SvO₂ using Equation (3), assuming a *Hct* of 40% and OEF was estimated from Equation (1) assuming SaO₂ of 100% in all participants. In addition, for the inter-session repeatability cohort, measured values of *Hct* from blood samples were also used to derive SvO₂ and SaO₂ was estimated as the mean of the five measurements taken from the pulse oximeter during the scan.

2.4.1 | Voxel size downsampling analysis

The impact of voxel size on different processing steps was determined by spatial downsampling of the 0.7 mm data in

image space prior to the four different processing steps described above: pre step 1 downsampling of the real and imaginary images directly output by the scanner, prior to phase unwrapping; pre step 2 downsampling of the total field map and the magnitude image, prior to background field removal; pre step 3 downsampling of the background field removal corrected local field map and the magnitude image, prior to dipole inversion; and pre step 4 downsampling of the quantitative susceptibility maps prior to the vein identification and OEF extraction process outlined above. Downsampling was achieved by partitioning the 0.7 mm high resolution image into cubic regions of $n \times n \times n$ adjacent voxels for $n = 2, 3, 4$, and creating a lower isotropic resolution image (voxel sizes of 1.4 mm, 2.1 mm, and 2.8 mm) of the mean intensity within the region.

2.5 | Statistical analysis and data comparisons

Statistical analyses were conducted using R 3.6.0 (R Core Team, 2019).

2.5.1 | Impact of voxel size and final echo time on OEF estimation

The impact of voxel size mediated by vein location on OEF was evaluated using a linear mixed model and analysis of variance (ANOVA). Voxel size (as a factor), the interaction of voxel size and vein location (deep or superficial), and vein identity were modelled as fixed effects, while subject was set as a random effect. Vein identity is included as a factor as it is expected that each vein may have different OEF due to size and/or region drained, and subject is included as there is likely to be a global difference in OEF between people. Likewise, the impact of final echo time mediated by vein location on OEF was evaluated using a similar model but replacing voxel size with final echo time. To evaluate further the impact of vein size on OEF estimation we considered the relationship between cross-sectional area (detailed in Supporting Information Text S1, which is available online) and OEF at different voxel sizes. Assuming that the estimate from the 0.7 mm voxel size data is the most accurate, we considered the error in OEF in relation to the 0.7 mm value (ΔOEF) as a function of cross-sectional area. We fitted an empirical mono-exponential function to this data using the `fminsearch` function in Matlab as a simple visual guide. A monoexponential function was chosen in preference to a linear fit as the line must asymptote to zero for large veins.

OEF estimates from the pre step 1 downsampled images (downsampling immediately after acquisition) were compared with OEF estimates from data acquired at different

resolutions. The final OEF estimates from the acquired data were linearly interpolated in order to estimate acquired data OEF values for 1.4, 2.1, and 2.8 mm voxels to account for the small discrepancies in downsampled and acquired voxel sizes (eg, 2 mm acquired vs 2.1 mm downsampled). These data were then compared with the pre step 1 downsampled OEF values to investigate whether this downsampled data follows a similar trend to the acquired data.

2.5.2 | Impact of voxel size within different QSM processing stages

To understand the sensitivity of each of the four processing steps to voxel size, the input images to each processing step were downsampled sequentially and the impact on OEF estimation investigated. The impact of voxel size at each processing stage, mediated by vein location, on OEF was evaluated using a linear mixed effect model and ANOVA. The dependent variable was OEF calculated from both data acquired at different resolutions and from the highest resolution data spatially downsampled at different processing stages. Factors were voxel size (0.7, 1.4, 2.1, or 2.8 mm) at acquisition and during each of the four processing steps and the interaction of each of these with vein location (deep or superficial). As before, vein identity was modeled as a fixed effect, and subject as a random effect. The purpose of this analysis is to determine during which of the four processing steps the voxel size has greatest impact on OEF estimation, specifically to identify whether the variance of the OEF estimates with voxel size for each processing step were significant, regardless of voxel size at earlier or subsequent processing steps.

2.5.3 | Intra- and inter-session repeatability

The intra-session repeatability was calculated as coefficient of variation ($\text{CoV}_{\text{intra}}$) of OEF from the seven repeat measurements on a single participant, and was estimated for each vein:

$$\text{CoV}_{\text{intra}} = 100 \cdot \frac{\sigma_{\text{intra}}}{\bar{x}_{\text{intra}}} \quad (4)$$

where \bar{x}_{intra} and σ_{intra} are the mean and SD of the OEF estimates from the seven repeat measurements, respectively. Veins were segmented separately for each repeat measurement.

The inter-session repeatability was estimated for each vein following the approach described by Bland and Altman,⁴¹ using:

$$\sigma_{\text{inter}} = \sqrt{\frac{\sum_{i=1}^{10} (x_{1i} - x_{2i})^2}{2n}} \quad (5)$$

where σ_{inter} is the within-subject standard deviation, n is the number of repeated measures (ie, 10 participants in this case), and x_{1i} and x_{2i} are the OEF estimates for each subject i at the first and second scan, respectively. The CoV was calculated as σ_{inter} divided by the mean OEF estimate over the 10 participants and expressed as a percentage. Inter-session repeatability was calculated using fixed SaO₂ of 100% and/or fixed *Hct* of 0.4 in parallel to use of the individual measurements from pulse oximetry and blood samples. To compare precision across the four approaches to OEF estimation (fixed SaO₂ & fixed *Hct*, measured SaO₂ & measured *Hct*, fixed SaO₂ & measured *Hct*, measured SaO₂ & fixed *Hct*), the OEF values calculated were compared using ANOVA, with vein identity, subject, and their interaction as factors. Residual mean square errors (MSEs) were compared as described in Supporting Information Text S2.

3 | RESULTS

3.1 | Impact of Voxel Size and final echo time on OEF estimation

All 11 veins were successfully identified, and their cross-sectional areas and diameters were measured in the highest resolution QSM maps for the four participants. OEF estimates were thus obtained in all veins for all participants at 0.7 mm resolution but 15 data points (out of 308 = 11 veins × 4 healthy volunteers × 7 voxel sizes, ie, 5%) were discarded at lower resolutions due to the presence of fewer than 10 non-zero voxels in the ROI (Supporting Information Table S1). The mean ± SE OEF measured at 0.7 mm across four participants ranged from 31.6 ± 3.0% (ISS) to 56.8 ± 0.7% (RTS), depending on the vein. Voxel size had a significant effect on OEF ($P < .0001$, Table 3), resulting in underestimation in OEF with increasing voxel size (Figure 2A,B). Interaction with vein location category was also significant ($P < .0001$), which can be seen in Figure 2 with (a) deep veins showing a greater voxel size dependence than (b) superficial veins. Final echo time had no significant effect on OEF and no interaction with vein location category (Table 3). Vein identity also accounted for significant variance in OEF, which may be due to vein size and/or different regional OEF.

To look further at the impact of voxel size on OEF, vein cross-sectional area was plotted against Δ OEF for different voxel sizes (Figure 3A). For voxel sizes of 1.5 mm or more, underestimation was greater in vessels with smaller diameters with larger differences observed from their values acquired at 0.7 mm. For a 1 mm voxel size, little difference in OEF estimation compared to 0.7 mm voxel size was observed except for vessels with cross-sectional area below approximately 20 mm² (small cerebral vein [SCV] and inferior sagittal sinus [ISS]), while for vessels above approximately 60 mm² (SSS and right transverse sinus [RTS]) it would appear that a 2 mm voxel size is sufficient. Figure 3C shows OEF

values using data downsampled from acquired data at 0.7 mm isotropic voxel size pre-processing step 1 with Figure 3B showing OEF estimates from acquired data interpolated to the same voxel size. It can be seen that the synthetic data do, in general, recapitulate the trends seen in the acquired data, confirming that further investigation of downsampling at different stages of processing is of potential value to identify the impact of voxel size at each processing stage.

3.2 | Impact of voxel size at different QSM processing stages

Twenty percent of the data points were discarded due to the presence of fewer than 10 voxels in the ROI as outlined in Supporting Information Table S2. Results of the ANOVA on the remaining data points are shown in Table 4 with plots of the significant effects shown in Figure 4. Voxel size has a significant impact on processing step 2, suggesting that voxel size is critical to accurate background field removal through the estimation of the background field map. Furthermore, the significance of the interaction between step 2 and vein location category confirms that the impact of voxel size on background field removal primarily impacts OEF estimation for superficial veins as illustrated in Figure 4C. Voxel size also has a significant impact on processing step 4 in which vein OEF estimates were calculated from the susceptibility map through ROI identification (Figure 4B). As before, vein identity also accounted for significant variance in OEF (Figure 4A). It was noted that this appeared to be related to cross-sectional area (shown with black crosses on Figure 4A), and a significant correlation was found between cross-sectional area and the OEF mean value model fits for each vein ($r = 0.77$, $P < .01$).

3.3 | Intra- and inter-session repeatability

In the healthy subject, the mean OEF over the seven repeats ranged from 27.9% (SCV) to 55.8% (LTS) depending on the vein. Intra-session precision of OEF was high (Table 5), with the coefficients of variation ranging from 2.1% to 4.8%.

In the participants with MCI, the OEF ranged from 25.5% to 51.5% depending on the veins. Bland-Altman analysis (Figure 5) yielded inter-session repeatability CoVs (Table 5) of 5.2% to 8.7%. No statistically significant differences were found between the residual MSEs calculated for any of the four options.

4 | DISCUSSION

In this study, we evaluate the impact of voxel size and final echo time on the estimation of regional OEF using QSM in

TABLE 3 Analysis of variance for the impact of voxel size, or final echo time mediated by vein location category (deep or superficial) on OEF estimation for all veins

Test 1	Df	SS	MS	F value	P value
Voxel size	6	7212	1202	21.7	<.0001
Vein identity	10	13135	1314	23.8	<.0001
Voxel size:category	6	3682	614	11.1	<.0001
Residual variance	55.3				
Test 2	Df	SS	MS	F value	P value
Final echo time	5	72	14	0.4	.87
Vein identity	10	16082	1608	40.8	<.0001
Final echo time:Category	5	83	17	0.4	.83
Residual variance	39.4				

Abbreviations: Df (degrees of freedom), SS (Sum of Squares), MS (Mean squares).

order to minimize acquisition time in four healthy subjects. We also assess the inter-session repeatability in 10 participants with MCI, as well as the intra-session repeatability in a single healthy subject. OEF estimates obtained using a voxel size of 0.7 mm were in good agreement with results reported elsewhere in healthy subjects.⁴² Eleven veins of varying geometries, locations, and orientations were selected on the basis of their large size and prominence. Only the six largest veins were used in the intra- and inter-repeatability study with voxel size 1 mm as other veins could not be reliably identified across all subjects as a consequence of the larger voxel sizes, brain masking, background field removal errors, or anatomic variation across individuals. Mean OEF values in the participants with MCI were in agreement with the literature.^{7,43}

The broad range of voxel sizes and final echo times chosen reflected those likely to be used in a clinical environment. We observed a significant influence of voxel size on OEF estimation (Figure 2A), dependent on vessel size (Figure 3A). The decrease in OEF estimates with increasing voxel size observed in deep veins, such as the SS, is mostly explained by partial volume effects (Table 4 and Figure 4). Voxel sizes larger than the vein diameter yield erroneous OEF values since they do not contain only blood, as do voxels that are smaller than vein diameter located at the vein boundary. The ratio between the number of boundary voxels (with lower susceptibility) to blood-only voxels (with higher susceptibility) increases with increasing voxel size, causing underestimation of OEF (Equation 2). We attempted to reduce this effect by considering the 90th percentile of susceptibility values in the ROI rather than the mean or median. Although the voxel within this ROI with the maximum susceptibility is the least likely to suffer from partial volume effects, the reliance on a single voxel would be vulnerable to noise, therefore, we opted to use the 90th percentile instead. This is less effective for thinner veins where even the voxel at the 90th percentile is likely to suffer from partial volume. The fact that in our downsampling simulations voxel size had the biggest and

most significant impact on OEF estimation at the final processing stage of extracting the ROI values from QSM images suggests that the impact of voxel size on OEF underestimation can indeed be almost entirely attributed to partial volume effects. Note that there is no significant impact of voxel size on the acquisition step, suggesting that any residual differences between the acquired and simulated data, such as Gibbs ringing and point spread function, are negligible, supported also by the similar trends seen for acquired and downsampled data in Figure 3B,C.

The volatile relationship between OEF and voxel size observed for veins located at the brain surface (Figure 2B), such as the SSS, may be due to several factors. A key consideration that motivates the classification of veins as deep or superficial is the presence of background field removal errors, which occur most prominently at the brain surface. These errors result from the failure of the operating principle of the background field removal method, which is used to distinguish the background field from the local field, producing an erroneous fringe pattern along the brain edge. Although we attempted to mitigate this by applying an upper susceptibility threshold and surface voxel erosion, this was only effective to remove voxels that clearly result in nonsensical susceptibility values, leaving other voxels that were more mildly affected within the ROI. For superficial vessels, larger voxel sizes may, therefore, have introduced erroneously high susceptibility values at the brain edge. The significant interaction in our downsampling simulation results between voxel size impact on background field removal and vein category (deep or superficial) (Table 4 and Figure 4C) supports the notion that background field removal errors are most critical at the brain surface and lead to erroneously high OEF estimates. Superficial veins, therefore, have competing impact of both partial volume and background field removal errors as voxel size increases, explaining the pattern of first lower and then, higher OEF estimates with increasing voxel size (Figure 2B).

We found that a 1 mm voxel size produces little difference in OEF estimation compared with 0.7 mm voxel size

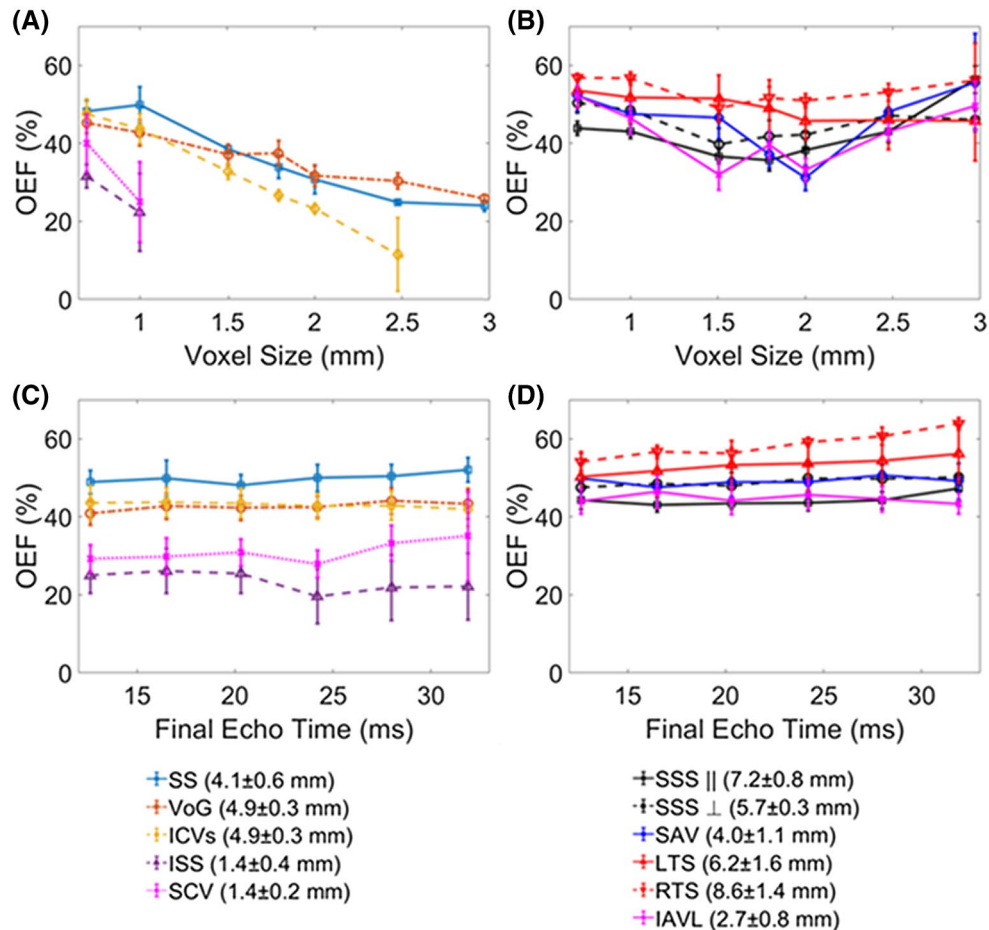


FIGURE 2 OEF estimation with increasing isotropic voxel size and final echo time. The top row shows the impact of voxel size on OEF estimation for deep veins (A) and superficial veins (B). The bottom row shows the impact of final echo time on OEF estimation for deep veins (C) and superficial veins (D). Estimates could not be made in some deep veins for the larger voxel sizes as there were fewer than 10 voxels in the ROI. Error bars represent standard error in the mean over the four healthy volunteers. Veins are identified in the key along with their diameters (mean \pm SD). SAV, superior anastomotic vein; LTS, left transverse sinus; IAVL, inferior anastomotic vein of Labbé

(Figure 3), except for vessels with cross-sectional area below approximately 20 mm^2 (diameter of $\sim 5.0 \text{ mm}$), such as the SCV and ISS, and has the benefit of reducing acquisition time from approximately 10 min to 4 min. Furthermore, for vessels above approximately 60 mm^2 (diameter of $\sim 8.7 \text{ mm}$), such as the SSS and RTS, it would appear that a 2 mm voxel size is sufficient, reducing acquisition time further to approximately 1 min. While it has become common practice to shorten acquisition time further using large slice thicknesses, this has recently been shown to lead to erroneous susceptibility estimates in tissue.⁴⁴ Moreover, increasing the voxel slice dimensions would be especially problematic when using QSM to estimate OEF in the veins, since the narrow profiles and often oblique orientations of veins would be difficult to image accurately. One limitation of our study is lack of a ground truth OEF value with residual partial volume effects likely to remain at 0.7 mm, especially in the smallest veins. Furthermore, we have not presented any method of correcting for the underestimation of OEF due to partial volume, rather presenting methods to avoid it through appropriate

choice of voxel size for the vein of interest. However, we note that other authors have suggested methods to compensate for partial volume effects. This can vary from a simple compensation factor included in Equation (3),^{22,45} to a novel method of SBO.⁴⁶ These may allow accurate estimation of OEF in smaller vessels or with larger voxels. However, care would be needed where the susceptibility of tissue outside the vessel may be altered and in the case of tortuous vessels.

The absence of a significant relationship between final echo time and OEF suggests that final echo times and, therefore, repetition times can be minimized by collecting as few as six bipolar echoes, or three unipolar echoes, down to a final echo time of at most 13 ms, which was the minimum we tested. The lack of a dependency suggests that 13 ms is sufficient to capture the deoxyhemoglobin-related signal decay and that longer final echo time is not beneficial in improving the accuracy of the phase estimates nor do additional echoes improve the precision. Our study was limited by a requirement of the software we used to generate our susceptibility maps (MEDI), which has a minimum requirement of three echoes, and as we analyzed odd and

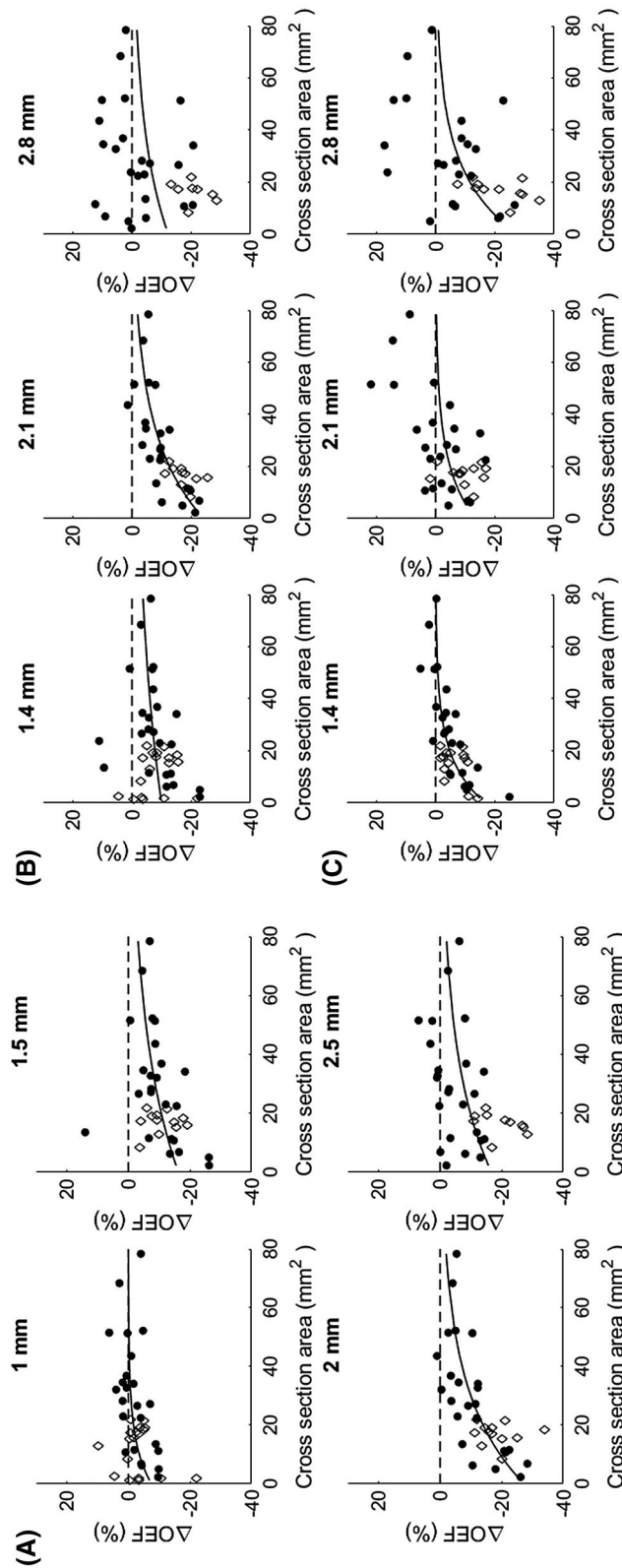


FIGURE 3 Influence of voxel size on OEF error (difference from 0.7 mm voxel size) as a function of vein cross-sectional area. Error in OEF compared to OEF estimate from 0.7 mm voxel size (Δ OEF), plotted against vein cross-sectional area, with an exponential fit. Each data point represents a single vein in one individual. Deep veins are shown as black circles and superficial veins as diamonds. OEF error is shown for: data acquired at 1 mm, 1.5 mm, 2 mm, and 2.5 mm isotropic voxel size (A); data interpolated from acquired data at 1 mm, 1.5 mm, 2 mm, 2.5 mm, and 3.0 mm to 1.4 mm, 2.1 mm, and 2.8 mm to aid comparison with downsampling acquired data (B); and OEF values created by downsampling acquired data at 0.7 mm isotropic voxel size pre-processing step 1 (C)

Test	Df	SS	MS	F value	P value
Main effects					
Acquisition	3	326	109	2.0	.11
Processing step 1: phase unwrapping	3	35	12	0.2	.89
Processing step 2: background field removal	3	487	162	3.0	.03
Processing step 3: dipole inversion	3	124	41	0.8	.52
Processing step 4: ROI identification and OEF estimation	3	5390	1797	33.0	<.0001
Vein identity	10	8730	873	16.1	<.0001
Interactions					
Vein location category by acquisition	3	176	59	1.1	.36
Vein location category by processing step 1	3	89	30	0.5	.65
Vein location category by processing step 2	3	657	219	4.0	.008
Vein location category by processing step 3	3	20	7	0.1	.95
Vein location category by processing step 4	3	38	13	0.2	.88

Abbreviations: Df, degrees of freedom; SS, sum of squares; MS, mean squares.

even echoes separately, we therefore needed at least six bipolar echoes. This nonetheless resulted in significant time saving, as we were able to halve the acquisition times using a final echo time of 12.6 ms rather than 31.9 ms (Table 1).

There are a number of limitations to our study. We neglected to include vessel orientation relative to B_0 as a factor, as we expected the impact to be small.^{27,47} We note, however, that this may have played a role in the heterogeneity of our OEF values across vein identity (Figure 4A). Moreover, these differences in OEF between veins may have a physiological basis, and the indication of reduced OEF in deep veins is supported by previous work.⁴⁸ While flow compensation was included in the frequency and slice-encoding directions, it was not incorporated in the phase-encoding direction that may have led to flow-related artifacts and associated errors in susceptibility estimates. However, as phase-encoding gradient amplitudes are relatively small, this is less important. Furthermore, such artifacts would be expected to get worse with increasing echo time.⁴⁹ We see no obvious change in flow-related displacement artifacts with increasing echo time (Supporting Information Figure S1), and the lack of association between final echo time and susceptibility values (Figure 2) suggests this did not affect our susceptibility estimates significantly. Prior to any image processing, each acquired dataset was partitioned by echo polarity with odd or even echo datasets analyzed separately. This was necessary as bipolar readout gradients were used which,

TABLE 4 Analysis of variance for the impact of voxel size at each processing stage, mediated by vein location category^a Deep or superficial, on OEF estimation for all veins.

due principally to differences in eddy currents between the gradient directions, manifests as phase discrepancies that led to catastrophic artifacts in the susceptibility maps when partitioning was not performed. Previous work has demonstrated effective correction for the differences in eddy currents enabling joint analysis of data with both polarities,⁵⁰ removing any potential spatial shifts between the odd and even echo polarity images. However, we did not observe such spatial shifts in our data (Supporting Information Figure S2) and, so, considered the averaging process to be adequate.

In this study, we assumed a fixed value of Hct and SaO_2 for all data processed from the four healthy volunteers. In reality, they are likely to vary within and across individuals. We accounted for this when estimating inter-session repeatability by measuring these parameters in the MCI cohort. We found that using individual measurements does not cause a loss in precision described by the inter-session CoV and residual MSE while potentially improving the accuracy of OEF estimates. The constant $\Delta\chi_{Hb-H_2O}$, which we used to calculate OEF, may also vary between individuals introducing additional error but this is likely to be very small.²⁰ The fact that intra-session CoVs, which were obtained in a younger person using fixed SaO_2 and Hct , were lower than inter-session CoVs, reflect additional sources of inter-session variability, and that could include: physiological change in OEF between sessions; differences in the acquisition and processing of the data, such

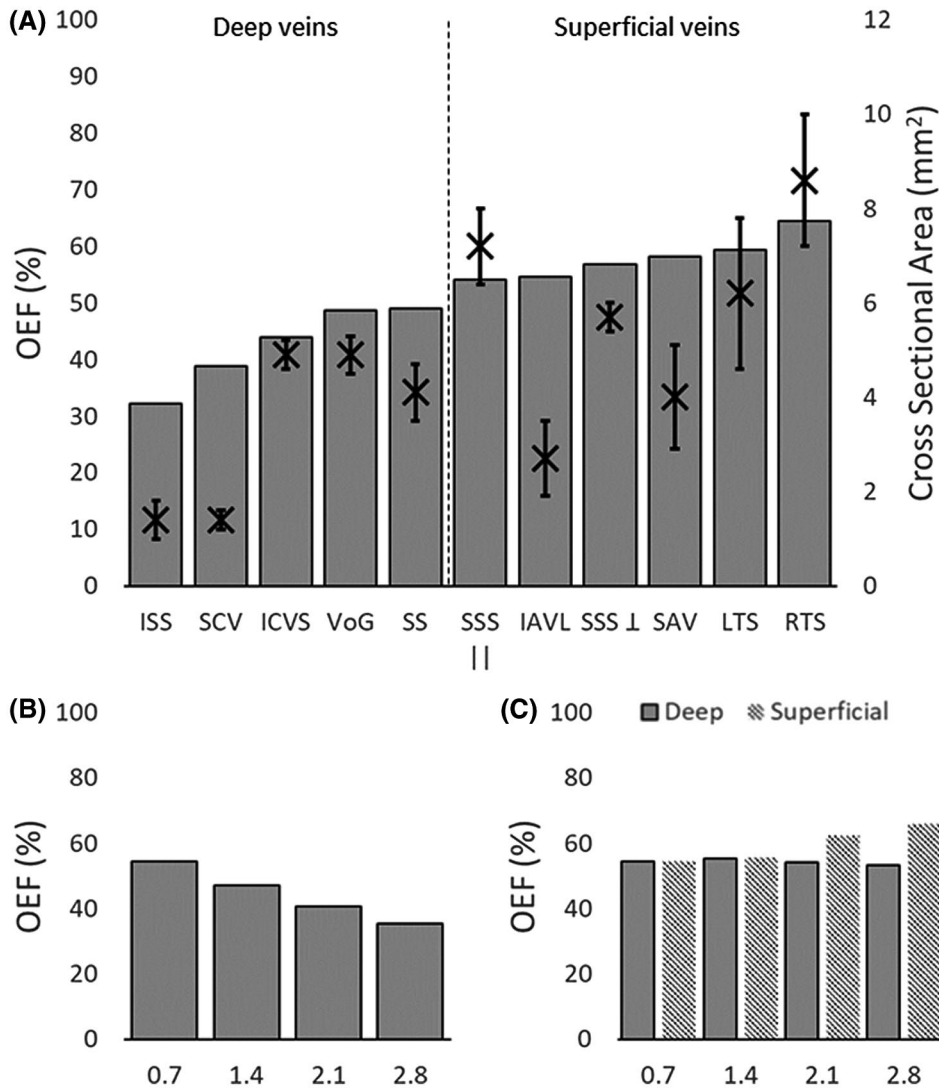


FIGURE 4 Impact of voxel size at different stages of QSM processing. Significant results from Table 4 are depicted regarding ANOVA of the impact of voxel size at each processing stage, mediated by vein location category (deep or superficial), with vein identity as a fixed effect. OEF mean value model fits are shown for vein identity (A); step 4, impact of voxel size on ROI identification and OEF extraction (B); and step 2, impact of voxel size on background field removal, dependent on vein location category (deep or superficial) (C). OEF varied with vein cross-sectional area (A, black x's, error bars are SDs) and superficial veins (SSS to RTS) have consistently higher OEF values. B, The dependence of OEF on voxel size was primarily due to the final step 4 of ROI identification and OEF extraction. C, Voxel size also had a significant impact on background field removal, but this was greater for superficial veins than deep veins. SAV, superior anastomotic vein; LTS, left transverse sinus; IAVL, inferior anastomotic vein of Labbé

TABLE 5 Coefficient of variation for OEF estimation

Estimate	SS	VoG	SSS ()	SSS (⊥)	ICVs	DTS
Intra-session	3.1	2.2	2.1	3.4	3.0	4.8
Inter-session						
Measured <i>SaO₂</i> & <i>Hct</i>	7.5	8.7	5.2	5.5	8.1	7.3
Measured <i>SaO₂</i> , <i>Hct</i> = 0.4	7.0	9.1	5.7	6.9	8.3	6.8
<i>SaO₂</i> = 100%, Measured <i>Hct</i>	6.5	8.2	4.4	4.6	6.5	6.1
<i>SaO₂</i> = 100%, <i>Hct</i> = 0.4	6.2	8.5	5.0	6.1	6.9	5.7

Abbreviation: DTS, dominant transverse sinus.

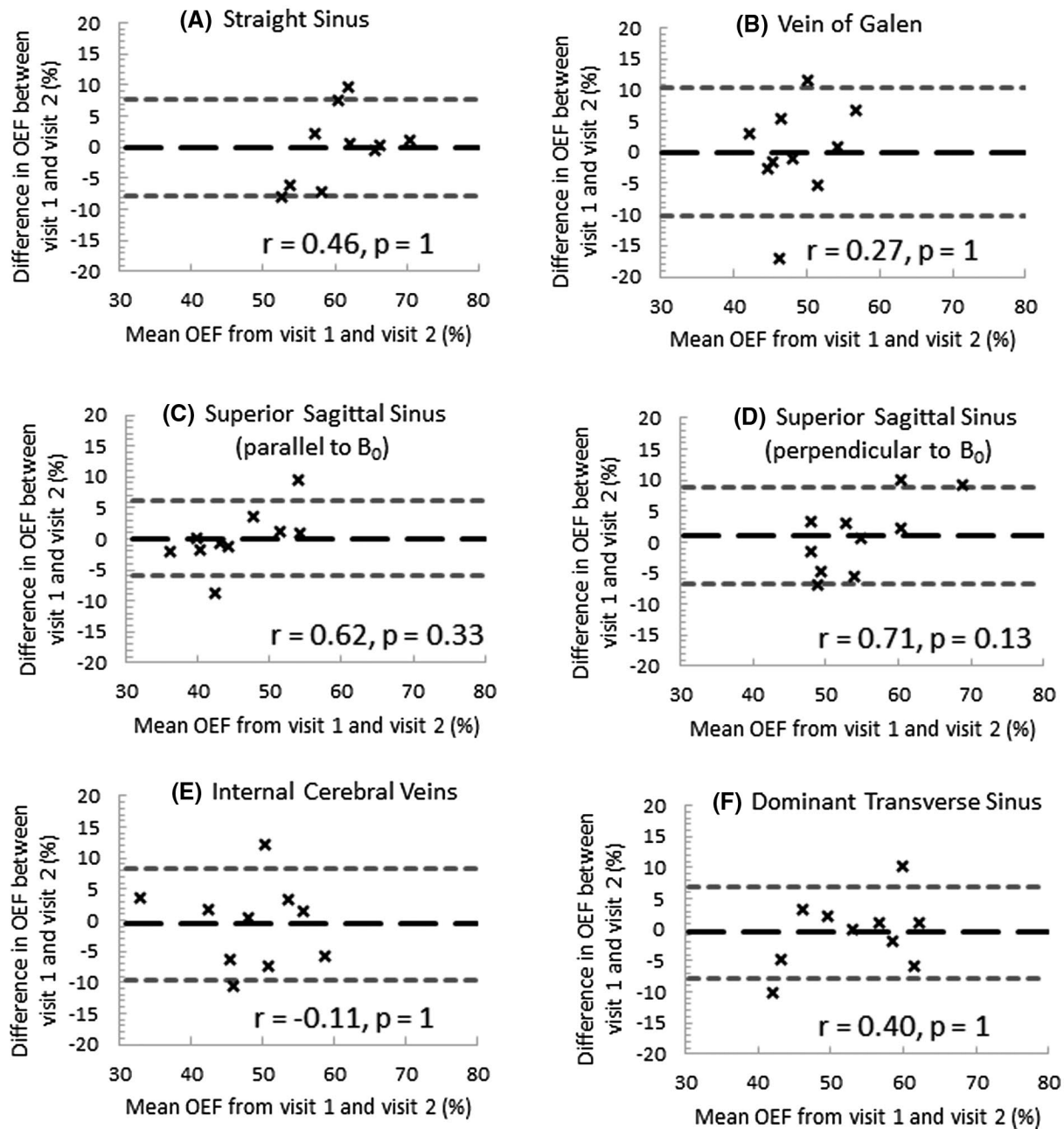


FIGURE 5 Bland-Altman plot of inter-session repeatability for OEF. Absolute differences between OEF estimates of both visits for each subject are plotted against the average of these estimates by region of interest: SS (A), VoG (B), (C) SSSII, SSS (D), ICV (E), and dominant transverse sinus (F). The long dotted line represents the mean difference between both visits across 10 participants, while the short dotted lines represent the 95% confidence interval. The r and P -values show the results of individual Pearson correlation testing which, after Bonferroni correction for multiple comparisons, are not significant

as positioning in the scanner and ROI location. Overall inter-session confidence intervals were comparable to those from similar studies.^{15,51} Liu et al¹⁵ used TRUST to obtain a coefficient of variation of 8.16% for intersession repeatability, to which our corresponding estimate (SSS segment parallel to B_0 , measured SaO_2 , fixed Hct) of 5.8% compares favorably. Moreover, our precision is worse than those obtained in a study using SBO of 2.3%.⁵² The whole brain coefficient of variation of 9.3% by Bremner et al⁵¹ using 15-O PET, which

is considered the gold standard imaging method for OEF, is also outside of the higher end of our findings.

5 | CONCLUSIONS

Regional QSM-OEF can be achieved in under 4 min across a wide range of vessels with cross-sectional area greater than 20 mm^2 using a final echo time of 12.6 ms and 1 mm isotropic

voxels. The use of larger voxels for major veins such as the SSS and RTS may be possible. However, this is complicated by the proximity of these vessels to the superficial surface of the brain where background field removal errors are more prominent.

ACKNOWLEDGMENTS

The authors thank the following organizations and individuals: GE Healthcare and the Engineering and Physical Sciences Research Council (EPSRC) (EP/M005909/1) for funding; Mark Symms (GE Healthcare), Amy Watkins, Ioannis Vamvakas, and other radiographers at the University of Manchester PET-MR suite; Pascal Spincemaille and the MEDI development team.

CONFLICT OF INTEREST


Maelene Lohezic is a former employee of GE Healthcare.

ORCID

John J. McFadden  <https://orcid.org/0000-0002-3034-6622>

Lauren A. Scott  <https://orcid.org/0000-0002-5423-0042>

Geoff J. M. Parker  <https://orcid.org/0000-0003-2934-2234>

Laura M. Parkes  <https://orcid.org/0000-0001-6488-507X>

Laura M. Parkes  <https://orcid.org/0000-0001-6488-507X>

Laura M. Parkes  <https://orcid.org/0000-0001-6488-507X>

REFERENCES

- Ishii K, Kitagaki H, Kono M, Mori E. Decreased medial temporal oxygen metabolism in Alzheimer's disease shown by PET. *J Nucl Med*. 1996;37:1159.
- Ibaraki M, Shimosegawa E, Miura S, et al. PET measurements of CBF, OEF, and CMRO 2 without arterial sampling in hyperacute ischemic stroke: method and error analysis. *Ann Nucl Med*. 2004;18:35-44.
- Kitamura S, Ujike T, Kuroki S, et al. Cerebral blood flow and oxygen metabolism in patients with Parkinson's disease. *Brain and Nerve*. 1988;40:979-985.
- Alsop DC, Detre JA, Golay X, et al. Recommended implementation of arterial spin-labeled perfusion MRI for clinical applications: a consensus of the ISMRM perfusion study group and the European consortium for ASL in dementia. *Magn Reson Med*. 2015;73:102-116.
- Yablonskiy DA, Sukstanskii AL, He X. Blood oxygenation level-dependent (BOLD)-based techniques for the quantification of brain hemodynamic and metabolic properties—theoretical models and experimental approaches. *NMR Biomed*. 2013;26:963-986.
- Aanerud J, Borghammer P, Chakravarty MM, et al. Brain energy metabolism and blood flow differences in healthy aging. *J Cereb Blood Flow Metab*. 2012;32:1177-1187.
- Nagata K, Maruya H, Yuya H, et al. Can PET data differentiate Alzheimer's disease from vascular dementia? *Ann NY Acad Sci*. 2000;903:252-261.
- Frackowiak RSJ, Lenzi G-L, Jones T, Heather JD. Quantitative measurement of regional cerebral blood flow and oxygen metabolism in man using ¹⁵O and positron emission tomography: theory, procedure, and normal values. *J Comput Assist Tomogr*. 1980;4:727-736.
- Bulte DP, Kelly M, Germuska M, et al. Quantitative measurement of cerebral physiology using respiratory-calibrated MRI. *Neuroimage*. 2012;60:582-591.
- Gauthier CJ, Hoge RD. A generalized procedure for calibrated MRI incorporating hyperoxia and hypercapnia. *Hum Brain Mapp*. 2013;34:1053-1069.
- Wise RG, Harris AD, Stone AJ, Murphy K. Measurement of OEF and absolute CMRO2: MRI-based methods using interleaved and combined hypercapnia and hyperoxia. *Neuroimage*. 2013;83:135-147.
- He X, Yablonskiy DA. Quantitative BOLD: mapping of human cerebral deoxygenated blood volume and oxygen extraction fraction: default state. *Magn Reson Med*. 2007;57:115-126.
- Liu P, Dimitrov I, Andrews T, et al. Multisite evaluations of a T2-relaxation-under-spin-tagging (TRUST) MRI technique to measure brain oxygenation. *Magn Reson Med*. 2016;75:680-687.
- Jiang D, Liu P, Li Y, Mao D, Xu C, Lu H. Cross-vendor harmonization of T2-relaxation-under-spin-tagging (TRUST) MRI for the assessment of cerebral venous oxygenation. *Magn Reson Med*. 2018;80:1125-1131.
- Liu P, Xu F, Lu H. Test-retest reproducibility of a rapid method to measure brain oxygen metabolism. *Magn Reson Med*. 2013;69:675-681.
- Thomas BP, Sheng M, Tseng BY, et al. Reduced global brain metabolism but maintained vascular function in amnesic mild cognitive impairment. *J Cereb Blood Flow Metab*. 2017;37:1508-1516.
- Ge Y, Zhang Z, Lu H, et al. Characterizing brain oxygen metabolism in patients with multiple sclerosis with T2-relaxation-under-spin-tagging MRI. *J Cereb Blood Flow Metab*. 2012;32:403-412.
- O'Brien C, Okell TW, Chiew M, Jezzard P. Volume-localized measurement of oxygen extraction fraction in the brain using MRI. *Magn Reson Med*. 2019;82:1412-1423.
- Wehrli FW, Fan AP, Rodgers ZB, Englund EK, Langham MC. Susceptibility-based time-resolved whole-organ and regional tissue oximetry. *NMR Biomed*. 2017;30:e3495.
- Weisskoff RM, Kiihne S. MRI susceptometry: image-based measurement of absolute susceptibility of MR contrast agents and human blood. *Magn Reson Med*. 1992;24:375-383.
- Spees WM, Yablonskiy DA, Oswood MC, Ackerman JJH. Water proton MR properties of human blood at 1.5 Tesla: magnetic susceptibility, T1, T2, T, and non-Lorentzian signal behavior. *Magn Reson Med*. 2001;45:533-542.
- Kudo K, Liu T, Murakami T, et al. Oxygen extraction fraction measurement using quantitative susceptibility mapping: comparison with positron emission tomography. *J Cereb Blood Flow Metab*. 2016;36:1424-1433.
- Zhang J, Liu T, Gupta A, Spincemaille P, Nguyen TD, Wang Y. Quantitative mapping of cerebral metabolic rate of oxygen (CMRO 2) using quantitative susceptibility mapping (QSM). *Magn Reson Med*. 2015;74:945-952.
- Özbay PS, Rossi C, Kocian R, et al. Effect of respiratory hyperoxic challenge on magnetic susceptibility in human brain assessed by quantitative susceptibility mapping (QSM). *NMR Biomed*. 2015;28:1688-1696.
- Fan AP, Evans KC, Stout JN, Rosen BR, Adalsteinsson E. Regional quantification of cerebral venous oxygenation from MRI susceptibility during hypercapnia. *Neuroimage*. 2015;104:146-155.

26. Buch S, Ye Y, Haacke EM. Quantifying the changes in oxygen extraction fraction and cerebral activity caused by caffeine and acetazolamide. *J Cereb Blood Flow Metab.* 2017;37:825-836.
27. Fan AP, Bilgic B, Gagnon L, et al. Quantitative oxygenation venography from MRI phase. *Magn Reson Med.* 2014;72:149-159.
28. Zhou D, Cho J, Zhang J, Spincemaille P, Wang Y. Susceptibility underestimation in a high-susceptibility phantom: dependence on imaging resolution, magnitude contrast, and other parameters. *Magn Reson Med.* 2017;78:1080-1086.
29. Liu T, Wisnieff C, Lou M, Chen W, Spincemaille P, Wang Y. Nonlinear formulation of the magnetic field to source relationship for robust quantitative susceptibility mapping. *Magn Reson Med.* 2013;69:467-476.
30. de Rochefort L, Liu T, Kressler B, et al. Quantitative susceptibility map reconstruction from MR phase data using Bayesian regularization: validation and application to brain imaging. *Magn Reson Med.* 2010;63:194-206.
31. Liu Z, Spincemaille P, Yao Y, Zhang Y, Wang Y. MEDI+ 0: morphology enabled dipole inversion with automatic uniform cerebrospinal fluid zero reference for quantitative susceptibility mapping. *Magn Reson Med.* 2018;79:2795-2803.
32. Liu J, Liu T, de Rochefort L, et al. Morphology enabled dipole inversion for quantitative susceptibility mapping using structural consistency between the magnitude image and the susceptibility map. *Neuroimage.* 2012;59:2560-2568.
33. Liu T, Liu J, De Rochefort L, et al. Morphology enabled dipole inversion (MEDI) from a single-angle acquisition: comparison with COSMOS in human brain imaging. *Magn Reson Med.* 2011;66:777-783.
34. Jenkinson M, Beckmann CF, Behrens TEJ, Woolrich MW, Smith SM. Fsl. *Neuroimage.* 2012;62:782-790.
35. Kressler B, De Rochefort L, Liu T, Spincemaille P, Jiang Q, Wang Y. Nonlinear regularization for per voxel estimation of magnetic susceptibility distributions from MRI field maps. *IEEE Trans Med Imaging.* 2009;29:273-281.
36. De Rochefort L, Brown R, Prince MR, Wang YI. Quantitative MR susceptibility mapping using piece-wise constant regularized inversion of the magnetic field. *Magn Reson Med.* 2008;60:1003-1009.
37. Cusack R, Papadakis N. New robust 3-D phase unwrapping algorithms: application to magnetic field mapping and undistorting echoplanar images. *Neuroimage.* 2002;16:754-764.
38. Liu T, Khalidov I, de Rochefort L, et al. A novel background field removal method for MRI using projection onto dipole fields. *NMR Biomed.* 2011;24:1129-1136.
39. Jenkinson M, Bannister P, Brady M, Smith S. Improved optimization for the robust and accurate linear registration and motion correction of brain images. *Neuroimage.* 2002;17:825-841.
40. Nolte J. *The Human Brain and an Introduction to its Functional Anatomy.* Philadelphia, PA: Mosby; 2009.
41. Bland JM, Altman DG. Measurement error and correlation coefficients. *BMJ.* 1996;313:41.
42. Ishii K, Sasaki M, Kitagaki H, Sakamoto S, Yamaji S, Maeda K. Regional difference in cerebral blood flow and oxidative metabolism in human cortex. *J Nucl Med.* 1996;37:1086-1088.
43. Frackowiak RSJ, Pozzilli C, du Legg NJ, et al. Regional cerebral oxygen supply and utilisation in dementia: a clinical and physiological study with oxygen-15 and positron tomography. A clinical and physiological study with oxygen-15 and positron tomography. *Brain.* 1981;104:753-778.
44. Karsa A, Punwani S, Shmueli K. The effect of low resolution and coverage on the accuracy of susceptibility mapping. *Magn Reson Med.* 2019;81:1833-1848.
45. Haacke EM, Tang J, Neelavalli J, Cheng YCN. Susceptibility mapping as a means to visualize veins and quantify oxygen saturation. *J Magn Reson Imaging.* 2010;32:663-676.
46. McDaniel P, Bilgic B, Fan AP, Stout JN, Adalsteinsson E. Mitigation of partial volume effects in susceptibility-based oxygenation measurements by joint utilization of magnitude and phase (JUMP). *Magn Reson Med.* 2017;77:1713-1727.
47. Ward PGD, Fan AP, Raniga P, et al. Improved quantification of cerebral vein oxygenation using partial volume correction. *Front Neurosci.* 2017;11:89.
48. Krishnamurthy LC, Liu P, Ge Y, Lu H. Vessel-specific quantification of blood oxygenation with T2-relaxation-under-phase-contrast MRI. *Magn Reson Med.* 2014;71:978-989.
49. Xu B, Liu T, Spincemaille P, Prince M, Wang Y. Flow compensated quantitative susceptibility mapping for venous oxygenation imaging. *Magn Reson Med.* 2014;72:438-445.
50. Li J, Chang S, Liu T, et al. Phase-corrected bipolar gradients in multi-echo gradient-echo sequences for quantitative susceptibility mapping. *Magn Reson Mater Phys, Biol Med.* 2015;28:347-355.
51. Bremmer JP, van Berckel BNM, Persoon S, et al. Day-to-day test-retest variability of CBF, CMRO 2, and OEF measurements using dynamic 15 O PET studies. *Mol Imag Biol.* 2011;13:759-768.
52. Jain V, Langham MC, Wehrli FW. MRI estimation of global brain oxygen consumption rate. *J Cereb Blood Flow Metab.* 2010;30:1598-1607.

SUPPORTING INFORMATION

Additional Supporting Information may be found online in the Supporting Information section.

FIGURE S1 Evidence for lack of flow-related displacement artefacts. Top row: magnitude images at two different echo times from one of the volunteers scanned with the protocol described in the final row of Table 1. There is no obvious spatial displacement of veins at the longer echo time. Bottom row: Local field maps calculated from the phase images after phase unwrapping and background field removal. Field maps calculated using phase images up to TE = 16.5 ms (left, corresponding to data from row 2 of Table 1) and 31.9 ms (right, corresponding to data from the final row of Table 1) do not show any obvious differences relating to potential flow artefacts that might be expected to be worse at the longer echo time

FIGURE S2 QSM images for the even and odd echoes. Images are taken from one of the volunteers scanned with the protocol described in the final row of Table 1. There is no obvious displacement of veins on the QSM maps calculated using the even and odd echoes. Cross-hairs which are placed at the same voxel location in each image

TABLE S1 The number of participants (max 4) for whom a region was discarded due to an insufficient number of voxels, organised by vein and voxel size

TABLE S2 142 data points (out of 704—11 veins \times 4 healthy volunteers \times 4 resolutions \times 4 points of intervention ie, 20%) were discarded due to the presence of fewer than 10 voxels in the ROI or, in the case of the interpolated data, if either of the nearest neighbour acquired data had been excluded

How to cite this article: McFadden JJ, Matthews JC, Scott LA, Parker GJM, Lohézić M, Parkes LM.

Optimization of quantitative susceptibility mapping for regional estimation of oxygen extraction fraction in the brain. *Magn Reson Med*. 2021;86:1314–1329. <https://doi.org/10.1002/mrm.28789>